

Article

# Catalytic Decomposition of CH<sub>4</sub> to Hydrogen and Carbon Nanotubes Using the Pt(1)-Fe(30)/MCM-41 Catalyst

Ho Joon Seo 

Department of Chemical and Biomolecular Engineering, Chonnam National University, Yeosu 59626, Republic of Korea; hjseo@jnu.ac.kr

**Abstract:** The catalytic decomposition of CH<sub>4</sub> to H<sub>2</sub> and carbon nanotubes (CNTs) was investigated regarding Pt(1)-Fe(30)/MCM-41 and Fe(30)/MCM-41 using a fixed-bed flow reactor under an atmosphere. X-ray diffraction (XRD), X-ray photoelectron spectroscopy (XPS), scanning electron microscopy (SEM), energy dispersive spectroscopy (EDS), transmission electron microscope (TEM), and Raman spectroscopy were used to characterize the behavior of Pt(1)-Fe(30)/MCM-41 and Fe(30)/MCM-41. The hydrogen yield of Pt(1)-Fe(30)/MCM-41 was 3.2 times higher than that of Fe(30)/MCM-41. When 1 wt% of Pt was added to Fe(30)/MCM-41 (Mobil Composition of Matter No. 41), the atomic percentage of Fe2p increased from 13.39% to 16.14% and the core Fe2p<sub>1/2</sub> electron levels of Fe<sup>0</sup> and Fe<sup>2+</sup> chemically shifted to lower energies (0.2 eV and 0.1 eV, respectively) than those of Fe(30)/MCM-41. The Fe, Pt, Si, and O nanoparticles were uniformly distributed on the catalyst surface, and the average iron particle sizes of the Pt(1)-Fe(30)/MCM-41 and Fe(30)/MCM-41 were about 33.4 nm and 58.5 nm, respectively. This is attributed to the uniform distribution of the nano-sized iron particles on the MCM-41 surface, which was due to the suitable metal-carrier interaction (SMCI) between Fe, Pt, and MCM-41 and the high reduction degree of Fe due to the spillover effect of H<sub>2</sub> from Pt to Fe. Pt(1)-Fe(30)/MCM-41 produced multiwalled CNTs and bamboo-shaped CNTs with high crystallinity and graphitization degree using the tip-growth mechanism, with an I<sub>D</sub>/I<sub>G</sub> ratio of 0.93 and a C(101)/C(002) ratio of 0.64.

**Keywords:** methane decomposition; hydrogen; MWCNT; Fe; Pt; MCM-41



**Citation:** Seo, H.J. Catalytic Decomposition of CH<sub>4</sub> to Hydrogen and Carbon Nanotubes Using the Pt(1)-Fe(30)/MCM-41 Catalyst. *Catalysts* **2024**, *14*, 282. <https://doi.org/10.3390/catal14040282>

Academic Editors: Yuting Li, Lun An and Nikita Dewangan

Received: 25 March 2024

Revised: 17 April 2024

Accepted: 18 April 2024

Published: 20 April 2024

## 1. Introduction

The catalytic decomposition of CH<sub>4</sub> (CDM) has garnered considerable attention as a promising method for hydrogen production. It offers a clean energy source that does not emit CO<sub>x</sub> or other greenhouse gases, but produces only useful carbon materials, such as carbon nanotubes [1]. Methane is the main component of natural gas, and it is an endothermic reaction, as shown in Equation (1). However, CDM is difficult to implement because it is energy intensive and thermodynamically favors carbon formation, which rapidly deposits carbon on the catalyst surface and deactivates the catalyst.



Ashik et al. [2] proposed hydrogen production and CNT growth as follows.



**Copyright:** © 2024 by the author. Licensee MDPI, Basel, Switzerland. This article is an open access article distributed under the terms and conditions of the Creative Commons Attribution (CC BY) license (<https://creativecommons.org/licenses/by/4.0/>).



where S is active sites. CNT growth initially occurs by cracking C–H bonds at active sites on the catalyst surface, resulting in atomic carbon deposition, followed by the dissolution and diffusion of carbon into metal nanoparticles. Finally, carbon deposition, nucleation, and filament formation occur behind the metal nanoparticles. Surendran et al. [3] reported on the synthesis of MWCNTs, which have a diameter in the range of 13 nm and a d-spacing of 0.33 nm, carried out at a relatively low temperature of 700 °C using liquified petroleum gas (LPG) as a hydrocarbon source and the chemical vapor deposition method. Suelves et al. [4] reported that Fe-based catalysts doped with Mo were prepared and tested in the catalytic decomposition of methane (CDM) and tubular carbon nanostructures with high structural order were obtained using Fe-Mo catalysts, mainly as multiwall carbon nanotubes (MWCNTs) and bamboo carbon nanotubes.

However, the catalyst used for methane decomposition is rapidly deactivated due to carbon deposition. Activators such as CO<sub>2</sub> and O<sub>2</sub> are used for the regeneration of deactivated metal catalysts. Otsuka et al. [5] conducted a study on methane decomposition and regeneration using Ni/Al<sub>2</sub>O<sub>3</sub>, Ni/SiO<sub>2</sub>, Ni/TiO<sub>2</sub>, and Pd-Ni/SiO<sub>2</sub> catalysts. They theorized that if the carbon deposited on the catalyst after the catalytic decomposition of methane is oxidized to oxygen or carbon dioxide, there is no need to supply energy in the partial oxidation reaction of methane to produce synthesis gas, and there is no generation of carbon dioxide.

Precious metals, such as Pd, Pt, Ru, and Rh, are useful for maintaining high activity and stability in CDM, but their industrial use is unsuitable as they are expensive and scarce. Using group VIII 3d transition metals, such as Fe and Ni, is an industrially viable alternative with the benefits of low cost and high availability. Fe- and Ni-based catalysts can produce liquid hydrocarbons from CO and H<sub>2</sub> using the Fischer–Tropsch process [6]. They exhibit excellent initial catalytic activity, but carbon is quickly deposited on the catalyst surface and deactivates the catalyst [7–14]. Several strategies have been used to maintain the lifespan of 3D transition-metal-based group VIII catalysts and to prevent carbon deposition on the catalyst surface [15]. Using X-ray diffraction (XRD), Kutteri et al. [16] found that the crystal size of the bimetal catalyst was smaller than that of the single metal catalyst; they also reported that this was consistent with the increase in active sites. Naikoo et al. [17] reported that nickel, ruthenium, and platinum-based catalysts showed the highest activity and catalytic efficiency for carbon-free hydrogen synthesis in the methane thermal decomposition process. Pudukudy et al. [18] reported that the addition of Pt to Ni/CeO<sub>2</sub> enhanced the activity and stability in a CDM reaction as the reduction temperature of NiO was decreased by hydrogen spillover and the uniform distribution of fine particles on the catalyst through moderate metal–carrier interaction. Karimi et al. [19] reported that a nickel-based catalyst containing an alkali, alkaline earth metal, transition metal (Fe, Co, Cu), noble metal (Pd, Pt), and rare earth metal (La) as a promoter was used in CDM for hydrogen production. When a promoter is appropriately added to a catalyst, its interaction increases catalytic activity and prevents carbon deposition on the catalyst. Shah et al. [20] reported that an Fe-M (M = Pd, Mo, Ni) binary catalyst supported on aluminum in the CDM had significantly higher activity than a single metal catalyst supported by Fe, Pd, Mo, and Ni. In a previous report, the decomposition temperature of methane was reduced to 400–500 °C compared to non-catalytic pyrolysis. Binary catalysts are believed to maintain catalytic activity for a long time in CDM [21–30] and prevent carbon deposition on the catalyst surface. MCM-41 [31] has pores ranging in sizes from 2 nm to 50 nm in a uniform hexagonal arrangement and is widely used as a catalyst carrier and adsorbent because of its physical properties, which include thick walls and high thermal stability. MCM-41 is a mesoporous material that can be used as a carrier for a carbon decomposition reactions and is a better carrier of catalyst than ZSM-5 zeolite, which has micropores that easily deposit carbon.

Rahimpour et al. [32] reported that the performance of a Cu-Fe bimetallic catalyst mounted onto an MCM-41 support in RWGS was investigated, and that MCM-41's high specific surface area is advantageous for dispersing active metals and preventing their sintering. Lopez et al. [33] reported that when both K and Fe are incorporated as promoters into the Cu/MCM-41 catalyst, the reaction rate of syngas to oxygenated compounds is notably increased, especially for ethanol.

In this study, we investigated the effect of Pt in order to create a catalyst that maintained high activity and long-term stability in CDM. The catalysts used were characterized using XRD, XPS, SEM, EDS, TEM, and Raman spectroscopy. The catalysts were evaluated by performing catalyst performance tests in CDM using a fixed bed flow reactor under atmospheric pressure to obtain the CNTs and the hydrogen yield.

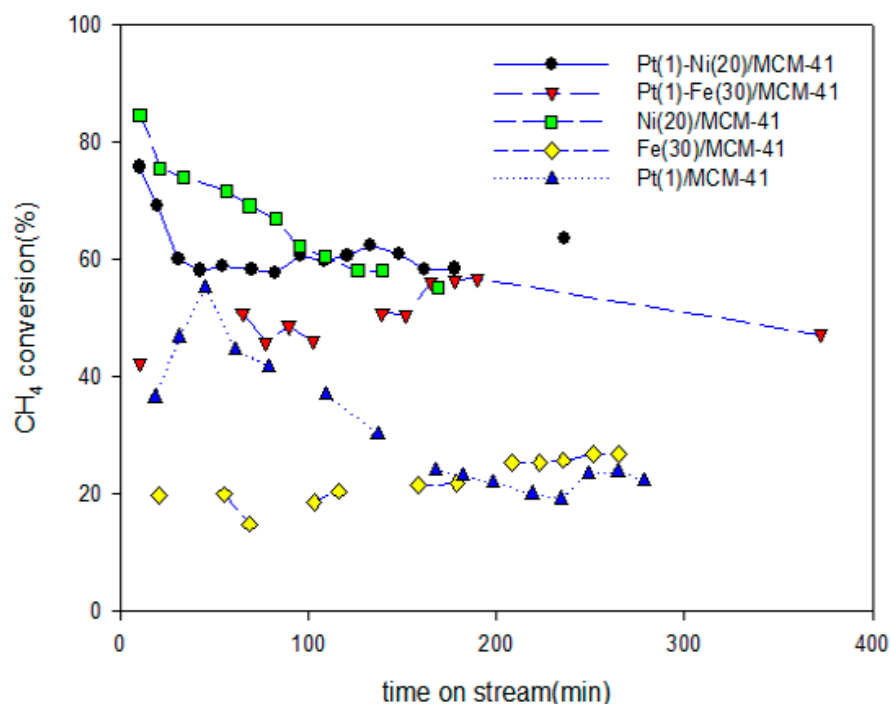
## 2. Results and Discussion

### 2.1. Activity of the Catalyst

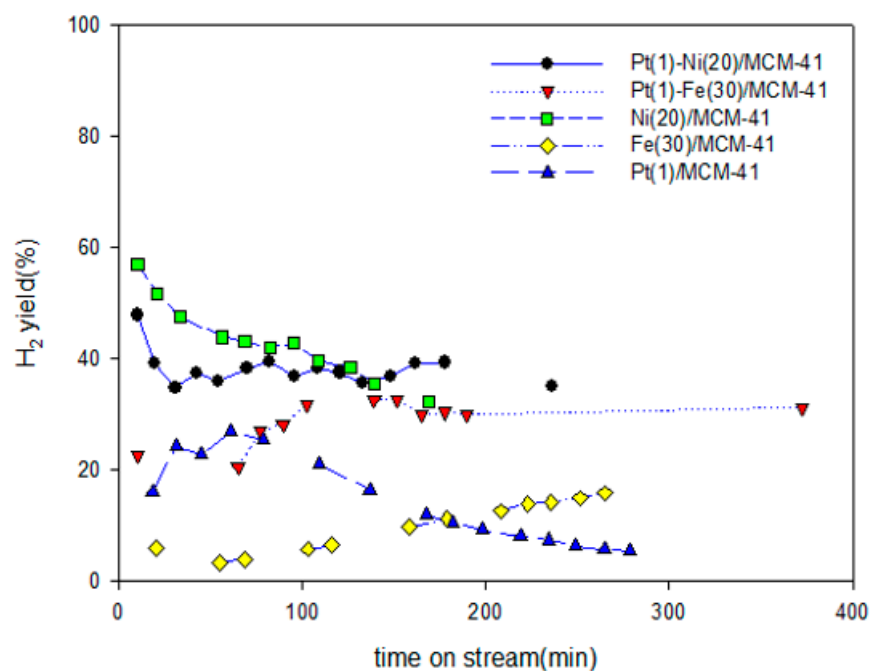
Figure 1 shows the methane conversion versus reaction time of CDM over the Fe(30)/MCM-41, Ni(20)/MCM-41, Pt(1)/MCM-41, Pt(1)-Fe(30)/MCM-41, and Pt(1)-Ni(20)/MCM-41 catalysts. The numbers in parentheses indicate the percentage of weight carried. The methane conversion of the Pt(1)-Ni(20)/MCM-41 catalyst was lower than that of the Ni(20)/MCM-41 catalyst up until 100 min; however, the methane conversion of the Pt(1)-Fe(30)/MCM-41 catalyst was significantly higher than that of the Fe(30)/MCM-41 catalyst. From ca. 100 min until ca. 165.2 min, the methane conversion of Pt(1)-Ni(20)/MCM-41 and Pt(1)-Fe(30)/MCM-41 exhibited an increasing trend, reaching about 58.2% and 56.2%, respectively. Additionally, the methane conversion of the Pt(1)/MCM-41 catalyst continued to increase until 44.8 min, reaching 55.2%; however, it decreased rapidly thereafter, reaching 22.3% at 288.5 min. The initial activity of Fe(30)/MCM-41, Ni(20)/MCM-41, Pt(1)-Fe(30)/MCM-41, and Pt(1)-Ni(20)/MCM-41 at about 102.5 min was in the following order: Ni(20)/MCM-41 > Pt(1)-Ni(20)/MCM-41 > Pt(1)-Fe(30)/MCM-41 >> Fe(30)/MCM-41. Upon adding 1 wt% Pt promoter to the Ni(20)/MCM-41 and Fe(30)/MCM-41 catalyst, the methane conversion data exhibited a nearly identical trend after 160 min. Additionally, the hydrogen yield of Fe(30)/MCM-41, Ni(20)/MCM, Pt(1)/MCM-41, Pt(1)-Fe(30)/MCM-41, and Pt(1)-Ni(20)/MCM-41 (Figure 2) also showed the same trend as the methane conversion, with a yield of 9.73, 32.33, 11.9, 29.9, 39.1%, respectively, obtained at 165.2 min, respectively. The addition of the 1 wt% Pt promoter to Ni(20)/MCM did not have a significant effect on the CDM hydrogen yield, but it had a significant effect on the Fe(30)/MCM-41. The hydrogen yield of the Pt(1)-Fe(30)/MCM-41 catalyst was 3.2 times higher than that of the Fe(30)/MCM-41 catalyst.

It is assumed that methane conversion and hydrogen yield can be improved by appropriate interactions between Fe or Ni, Pt, and MCM-41 [8], as well as by increasing the reduction degree of nano-sized Fe and Ni particles, which causes H<sub>2</sub> to spillover [34–39]. It is also believed that adding 1 wt% of Pt to Fe(30)/MCM-41 and Ni(20)/MCM-41 creates fine nano-sized Fe and Ni particles on the catalyst surface, facilitating uniform dispersion through the “dilution” effect of Pt atoms [34], which is attributed to an increase in dispersion of the Fe or Ni particles on the catalyst surface caused by intimate contact between Fe(30) or Ni(20) and Pt of 1 wt%.

Figure 3 shows the methane conversion and the hydrogen yield plotted against the reaction temperature of CDM over Pt(1)-Fe(30)/MCM-41. The methane conversion and the hydrogen yield gradually increased as the temperature increased. The methane conversion values were 22.18, 37.56, and 46.17% and the hydrogen yields were 12.32, 21.98, and 31.68%, respectively, at reaction temperatures of 823, 923, and 973 K. However, at high reaction temperatures of 973 and 1023 K, the methane conversion quickly increased to 46.17 and 64.40%, while the hydrogen yield gradually increased to 31.68 and 37.94%. From this phenomenon, it can be inferred that the carbon reaction rate of CDM proceeds more quickly than the hydrogen reaction rate at a high reaction temperature of 1023 K.



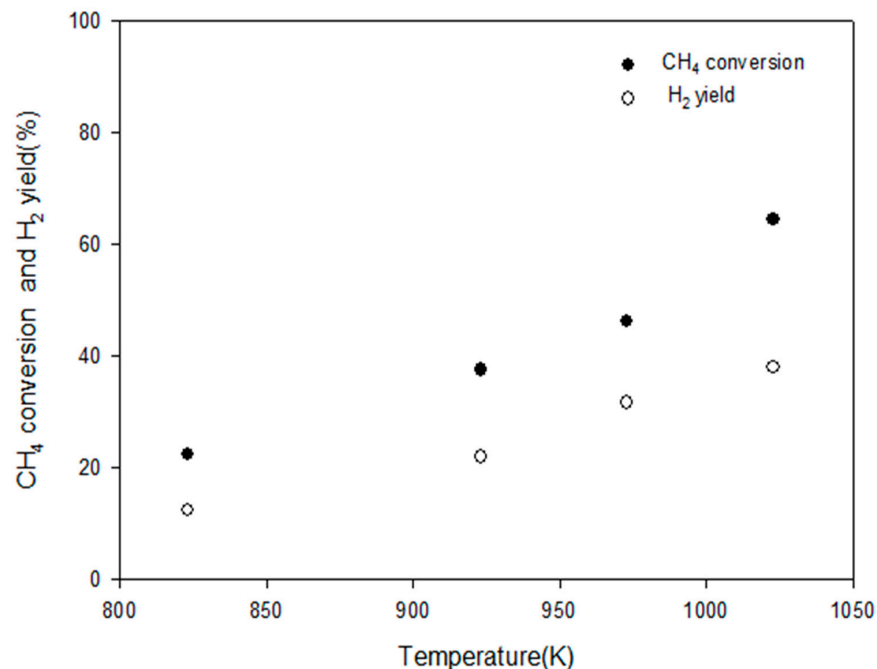
**Figure 1.** Conversion of  $\text{CH}_4$  obtained in methane decomposition over Pt(1)-Fe(30)/MCM-41, Pt(1)-Ni(20)/MCM-41, Fe(30)/MCM-41, Ni(20)/MCM-41, and Pt(1)/MCM-41 in the packed bed reactor:  $P = 1 \text{ atm}$ ,  $T = 700 \text{ }^\circ\text{C}$ , and  $\text{GHSV} = 4.2 \times 10^4 \text{ CH}_4 \text{ mL g}_{\text{cat.}}^{-1} \cdot \text{h}^{-1}$ .



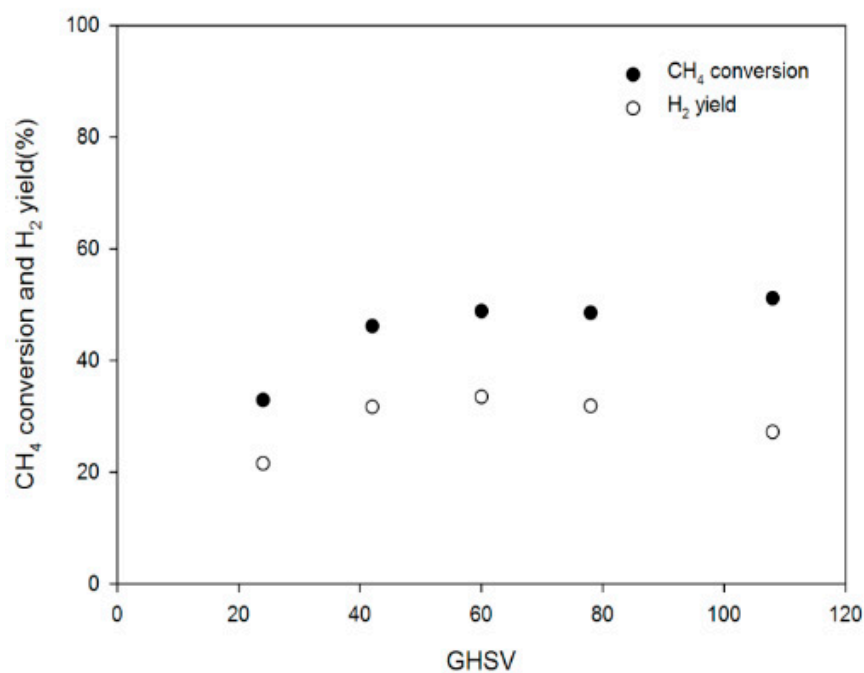
**Figure 2.** Yield of  $\text{H}_2$  obtained in methane decomposition over Pt(1)-Fe(30)/MCM-41, Pt(1)-Ni(20)/MCM-41, Fe(30)/MCM-41, Ni(20)/MCM-41, and Pt(1)/MCM-41 in the packed bed reactor:  $P = 1 \text{ atm}$ ,  $T = 700 \text{ }^\circ\text{C}$ , and  $\text{GHSV} = 4.2 \times 10^4 \text{ CH}_4 \text{ mL g}_{\text{cat.}}^{-1} \cdot \text{h}^{-1}$ .

Figure 4 shows the methane conversion and hydrogen yield plotted against the GHSV of the CDM over Pt(1)-Fe(30)/MCM-41. As the GHSV increased from 24 to 42  $\text{mL/g}_{\text{cat.}} \cdot \text{h}$ , the methane conversion rate and hydrogen yield increased linearly from 32.92% and 21.55% to 46.17% and 31.68%, respectively. However, as the GHSV increased from 60 to

78 mL/g<sub>cat.</sub>·h, methane conversion was almost constant from 48.83 to 48.52%, but the hydrogen yield decreased from 33.50% to 31.85%. Additionally, as the GHSV increased from 78 to 108 mL/g<sub>cat.</sub>·h, methane conversion gradually increased from 48.52% to 51.15%, but the hydrogen yield gradually decreased from 31.85% to 27.19%.



**Figure 3.** CH<sub>4</sub> conversion and H<sub>2</sub> yield vs. reaction temperature obtained in methane decomposition over Pt(1)-Fe(30)/MCM-41 in the packed bed reactor: P = 1 atm and GHSV =  $4.2 \times 10^4$  CH<sub>4</sub> mL g<sub>cat.</sub><sup>-1</sup>·h<sup>-1</sup>.



**Figure 4.** CH<sub>4</sub> conversion and H<sub>2</sub> yield vs. GHSV obtained in methane decomposition over Pt(1)-Fe(30)/MCM-41 in the packed bed reactor: P = 1 atm and T = 700 °C.

This phenomenon is attributable to rapid carbon deposition on the catalyst surface through the diffusion of carbon decomposed in CDM as the GHSV increases [40].

## 2.2. Characterization of the Fresh Catalyst

Figure 5 shows the XRD patterns of Pt(1)-Fe(30)/MCM-41 and Fe(30)/MCM-41 catalysts before reaction. Characteristic peaks of typical hexagonal  $\text{Fe}_2\text{O}_3$  at  $2\theta = 24.13^\circ, 33.10^\circ, 35.63^\circ, 40.83^\circ, 49.42^\circ, 53.98^\circ, 63.99^\circ, 75.44^\circ, 84.89^\circ,$  and  $88.48^\circ$  and those of cubic Pt at  $2\theta = 39.74^\circ, 46.22^\circ, 67.43^\circ, 81.22^\circ,$  and  $85.66^\circ$  were observed. However, the crystal phases of metals such as Fe, FeO, PtO, and  $\text{PtO}_2$ , and the characteristic peaks of dissimilar metals, such as PtFe, were not observed. Only in the crystalline phase did fine nano-sized particles of  $\text{Fe}_2\text{O}_3$  and Pt metal appear.

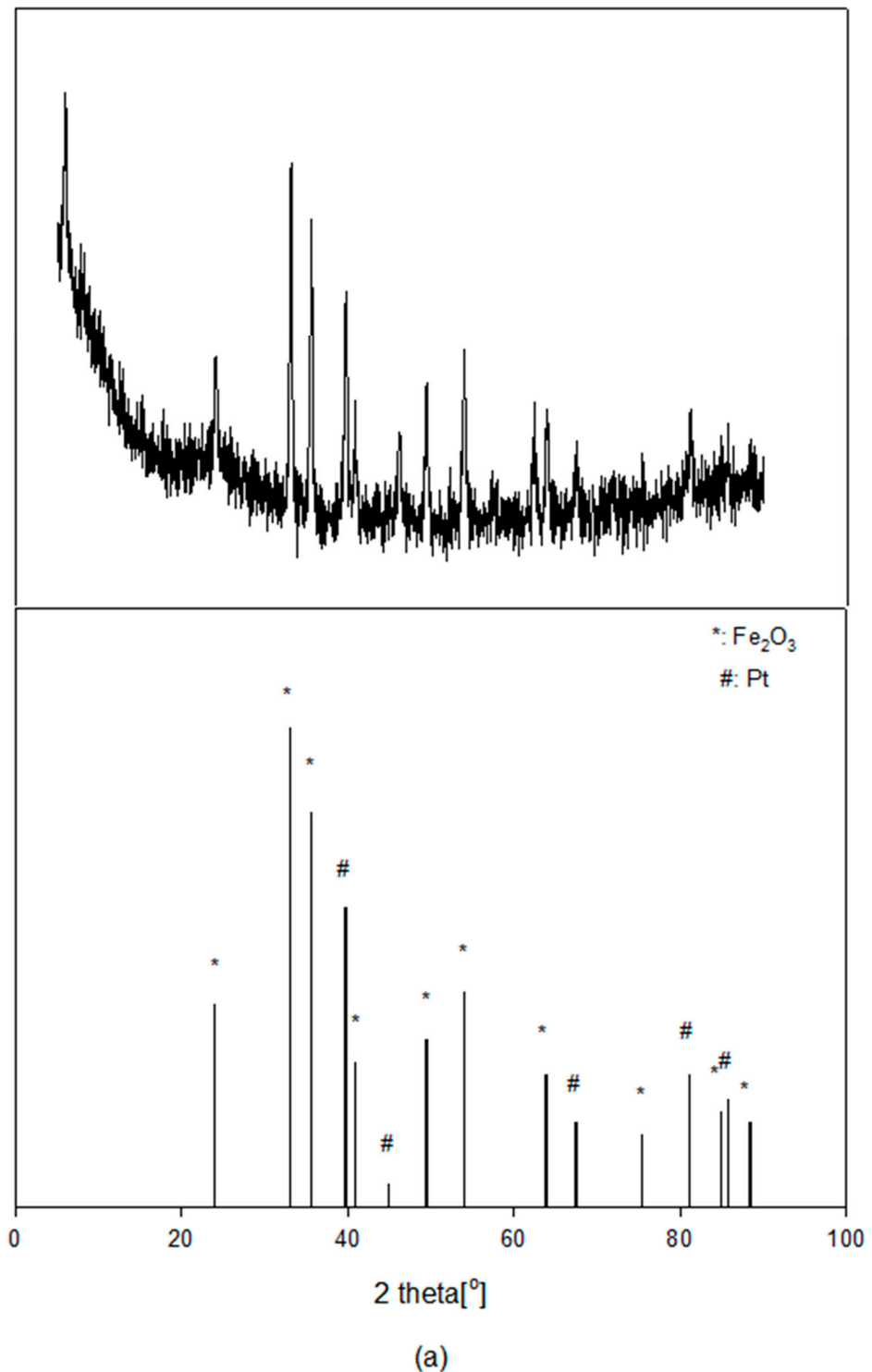
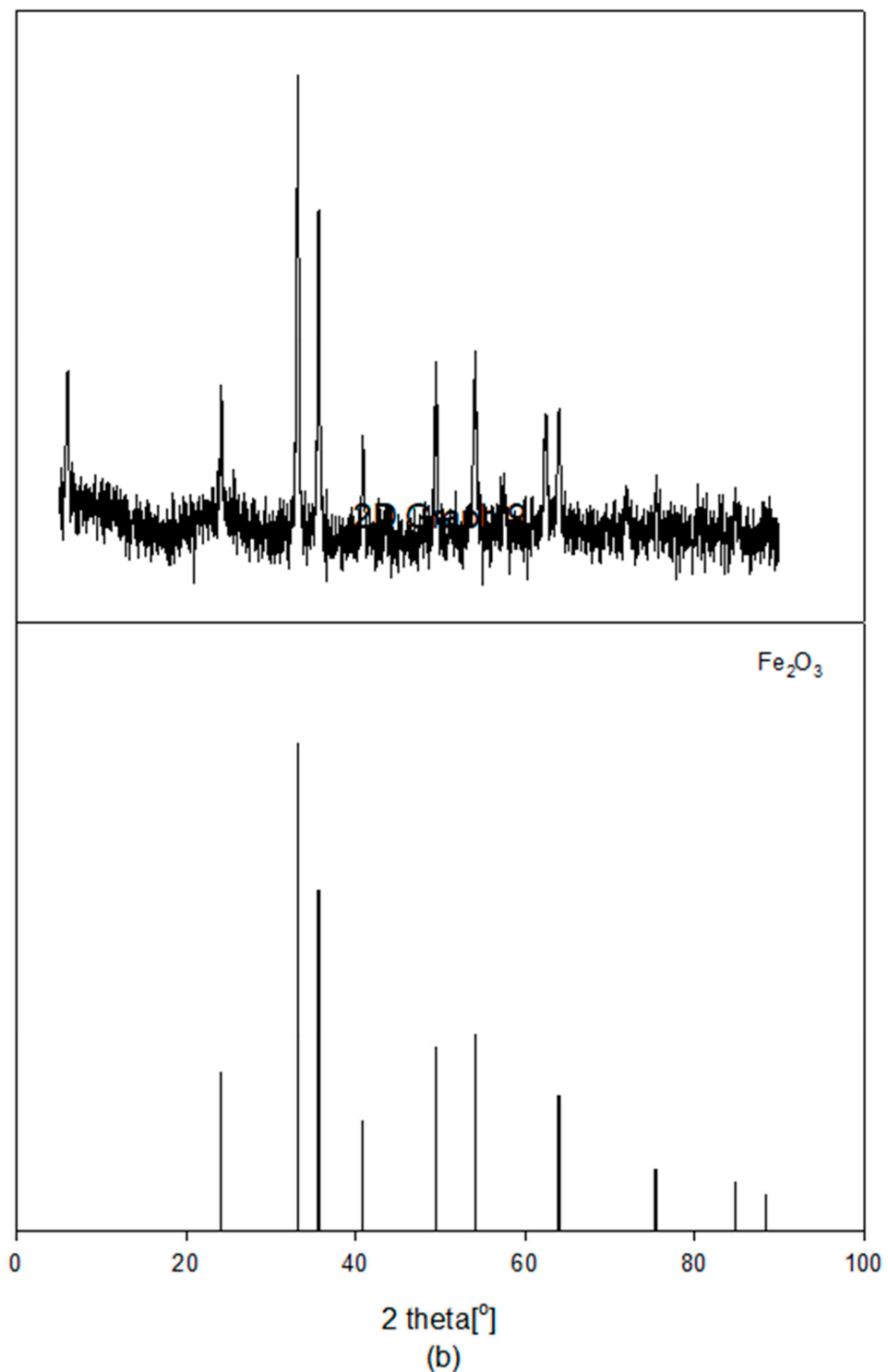


Figure 5. Cont.



**Figure 5.** XRD patterns of (a) fresh Pt(1)-Fe(30)/MCM-41 and (b) fresh Fe(30)/MCM-41 catalysts.

These behaviors suggested that the fine nano-sized Fe and Pt particles created by appropriate metal–carrier interactions were well dispersed in the MCM-41 carrier [8], and most Fe species in fresh Pt(1)-Fe(30)/MCM-41 were present as Fe<sub>2</sub>O<sub>3</sub> crystallite. This was also consistent with FESEM and EDS results.

Figure 6 shows the XPS spectra of Pt(1)-Fe(30)/MCM-41 and Fe(30)/MCM-41 at the core electron levels of (a) Pt4f, (b) Fe2p, (c) O1s, and (d) Si2p before reaction. Characteristic Pt4f<sub>7/2</sub> peaks appeared at 71.28, 72.68, and 74.68 eV, while those of Pt4f<sub>5/2</sub> appeared at 74.88, 76.28, and 78.08 eV. These characteristic peaks were Pt<sup>0</sup>, Pt<sup>2+</sup>, and Pt<sup>4+</sup>, respectively. The

characteristic peaks of Fe2p<sub>3/2</sub>, namely Fe<sup>0</sup>, Fe<sup>2+</sup>, and Fe<sup>3+</sup>, appeared at 709.58, 710.78, and 713.18 eV, respectively. The Fe<sup>2+</sup> satellite peak of Fe2p<sub>3/2</sub> appeared at 719.18 eV. Characteristic peaks of Fe2p<sub>1/2</sub>, namely Fe<sup>0</sup>, Fe<sup>2+</sup>, and Fe<sup>3+</sup>, appeared at 722.68, 724.28, and 726.78 eV, respectively. The Fe<sup>2+</sup> satellite peak of Fe2p<sub>1/2</sub> appeared at 723.38 eV. It was demonstrated that the satellite peaks of Fe2p<sub>3/2</sub> and Fe2p<sub>1/2</sub> stem from the combination of iron oxide and nanoparticles of Fe<sub>2</sub>O<sub>3</sub> and FeO [41]. The Fe2p intensity of Pt(1)-Fe(30)/MCM-41 was higher than that of Fe(30)/MCM-41. There was no change in the Fe2p<sub>3/2</sub> core electron levels of Pt(1)-Fe(30)/MCM-41, but the Fe2p<sub>1/2</sub> core electron levels of Fe<sup>0</sup> and Fe<sup>2+</sup> chemically shifted to lower energies (0.2 eV and 0.1 eV, respectively) than those of the Fe(30)/MCM-41. Characteristic peaks of O1s appeared at 529.88 and 533.18 eV, corresponding to O<sup>2-</sup> and O<sup>-</sup>, respectively. The O1s intensity of Pt(1)-Fe(30)/MCM-41 was lower than that of Fe(30)/MCM-41. However, the core electron levels of O1s chemically shifted slightly to higher energy levels. Characteristic peaks of Si2p<sub>3/2</sub> and Si2p<sub>1/2</sub> appeared at 103.78 and 104.38 eV, respectively, corresponding to Si<sup>4+</sup>. The Si2p intensity of Pt(1)-Fe(30)/MCM-41 was lower than that of Fe(30)/MCM-41, but the core electron levels of Si2p also chemically shifted slightly to a higher energy. It was concluded that Fe ions of Pt(1)-Fe(30)/MCM-41 are more easily reduced than those in Fe(30)/MCM-41 as electrons move from Fe ions to O or Si atoms; this is due to the spillover effect of hydrogen. Table 1 shows that when 1 wt% of Pt was added to the Fe(30)/MCM-41 catalyst, the atomic percentage of Fe2p on the catalyst surface increased from 13.39% to 16.14% owing to the synergistic effect of Fe and Pt with appropriate metal–support interaction; however, the atomic percentage of Si2p decreased from 86.6% to 82.34%. It can be inferred that Fe and Pt interact with the lattice oxygen of MCM-41 to create FeO, Fe<sub>2</sub>O<sub>3</sub>, PtO, and PtO<sub>2</sub> compounds, thereby changing the lattice constant of the catalyst and causing a synergistic effect between Pt, Fe, and MCM-41 as a result of appropriate metal–support interaction. Damyanova et al. [8] reported that adding 0.5 wt% of Pd to Ni/MCM-41 creates small nano-sized Ni particles, easily reduces NiO particles, and improves the dispersion of nickel particles on the catalyst surface. Karimi et al. [18] showed that the presence of Pt on the catalyst promotes the reduction degree of Ni and the dispersion of Ni on the carrier through a distinct spillover effect of H<sub>2</sub>.

**Table 1.** Atomic percentage of core electron levels for fresh Pt(1)-Fe(30)/MCM-41 and Fe(30)/MCM-41 according to XPS data [42].

Fresh Catalyst	Core Electron Levels	Atomic %
Pt(1)-Fe(30)/MCM-41	Pt4f	1.51
	Fe2p	16.14
	Si2p	82.34
Fe(30)/MCM-41	Fe2p	13.39
	Si2p	86.60

Figure 7 shows the FESEM images, and mapping as well as the EDS characteristic peaks of the Pt(1)-Fe(30)/MCM-41 and Fe(30)/MCM-41 catalysts. The presence of Fe, Pt, Si, and O nanoparticles on the catalyst surface was confirmed. The average particle size of Fe was about 58.5 nm for the Fe(30)/MCM-41 and about 33.4 nm for Pt(1)-Fe(30)/MCM-41. The particle size of the catalyst surface of the Pt(1)-Fe(30)/MCM-41 catalyst was found to be 1.8 times smaller than that of the Fe(30)/MCM-41 catalyst, and the spherical particles were uniformly distributed. It can be assumed that the addition of 1 wt% of Pt to Fe(30)/MCM-41 creates much smaller nano-sized iron particles, resulting in a higher dispersion on the MCM-41 surface due to the suitable metal–carrier interaction (SMCI) [12], which means that catalysis is enhanced when Pt, Fe metal nanoparticles supported on the surface of MCM-41 are properly chemically bonded to the carrier.

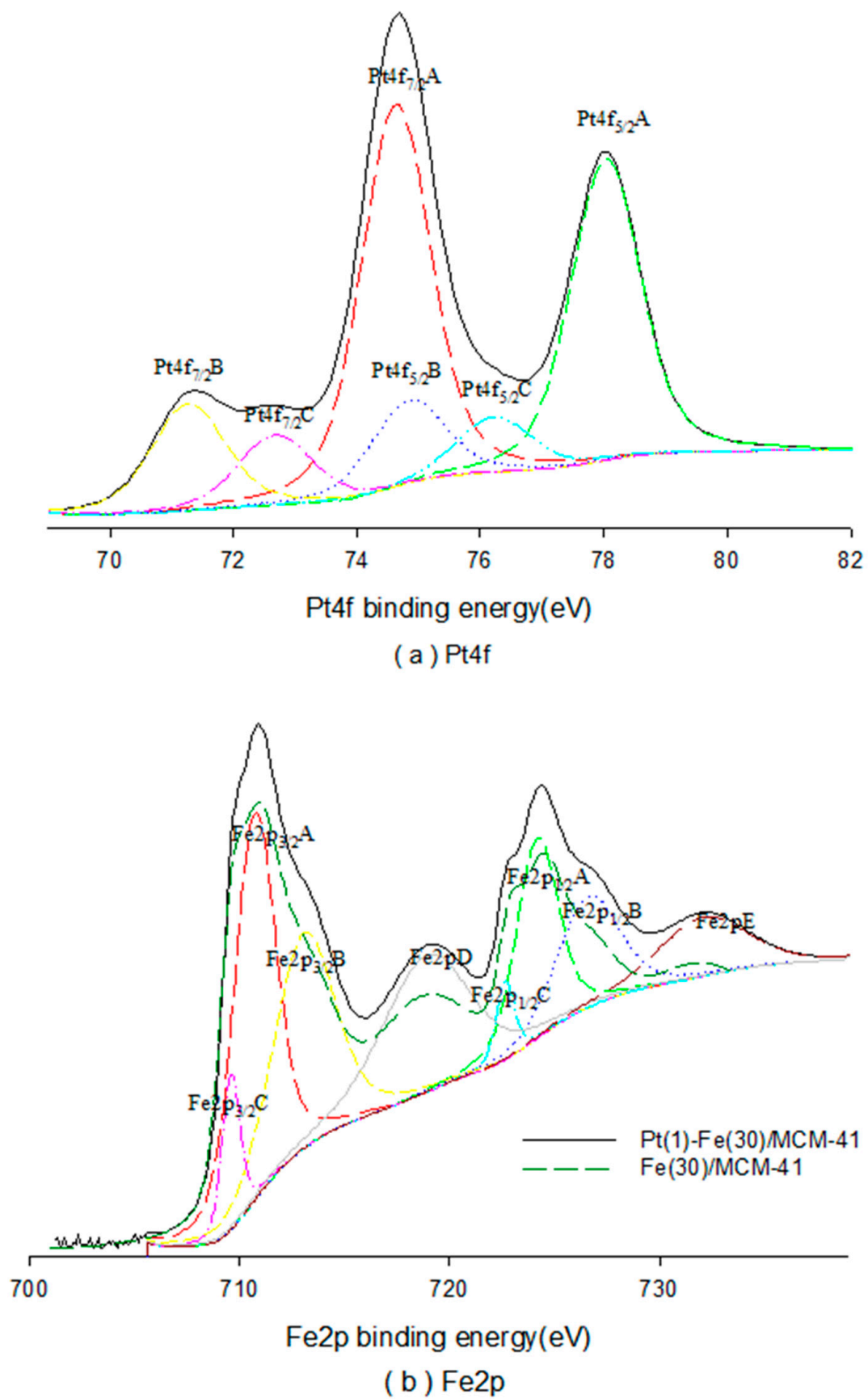
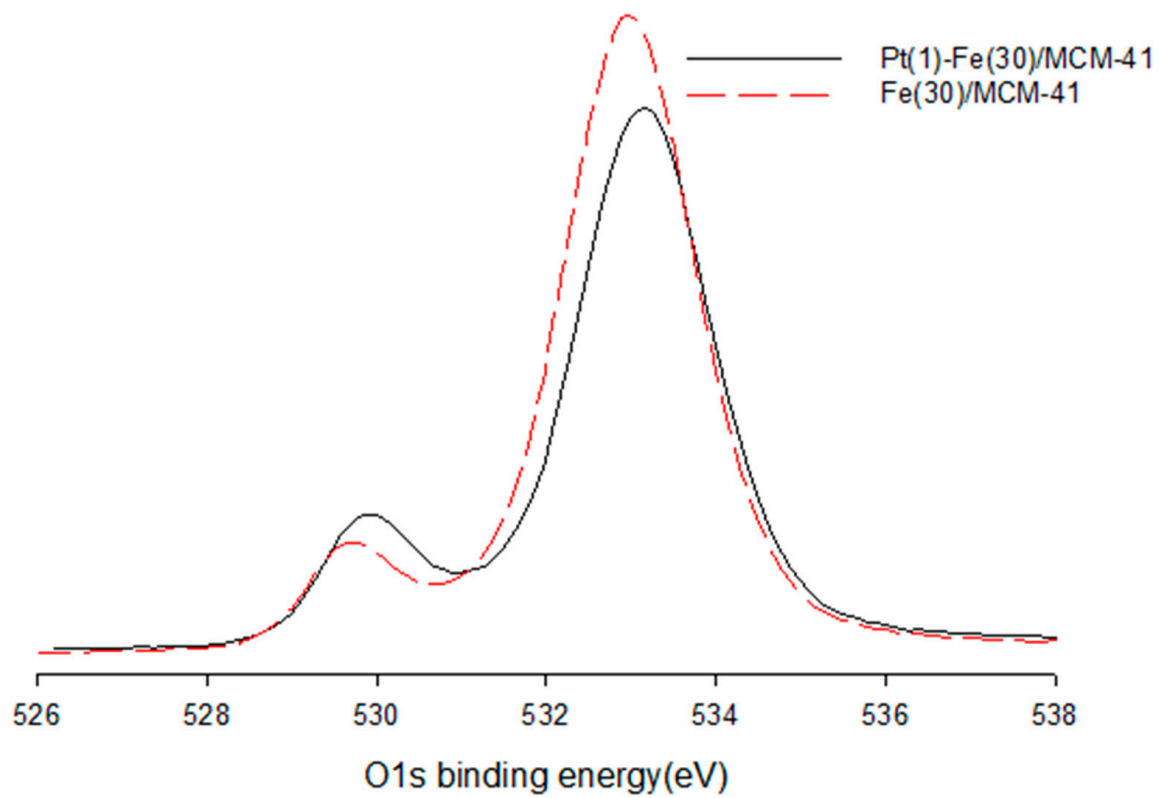
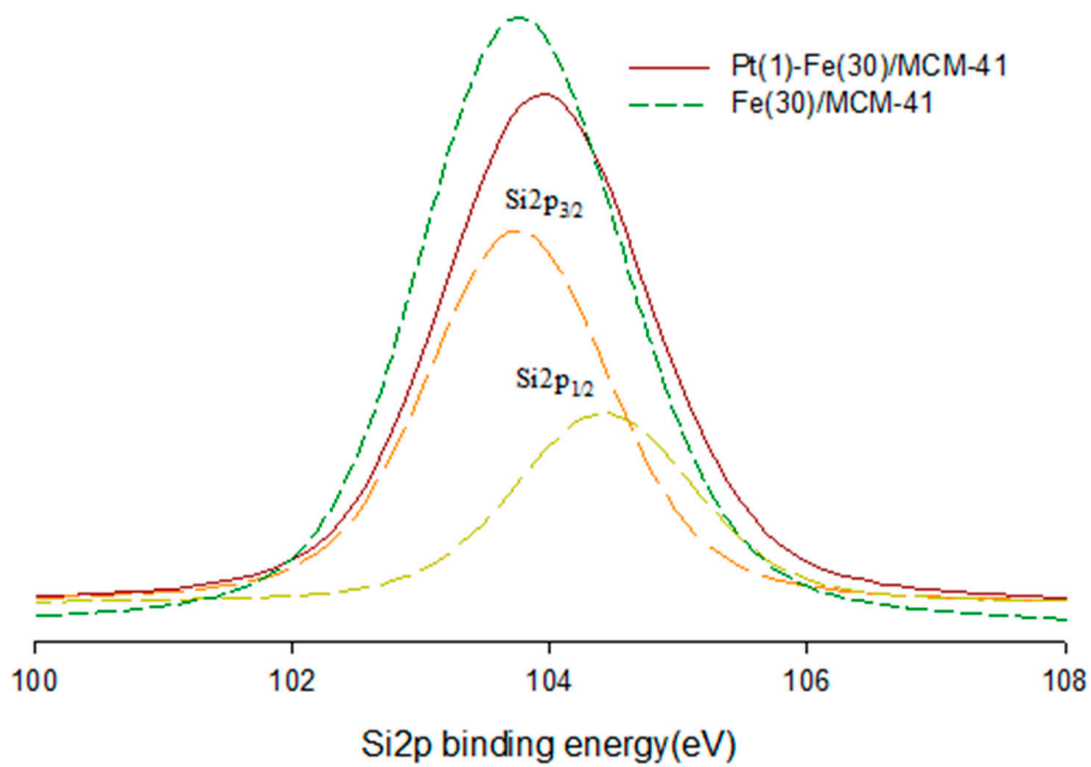


Figure 6. Cont.



(c) O1s



(d) Si2p

**Figure 6.** XPS spectra of (a) Pt4f, (b) Fe2p, (c) O1s, and (d) Si2p core electron levels for fresh Pt(1)-Fe(30)/MCM-41 and Fe(30)/MCM-41 [42].

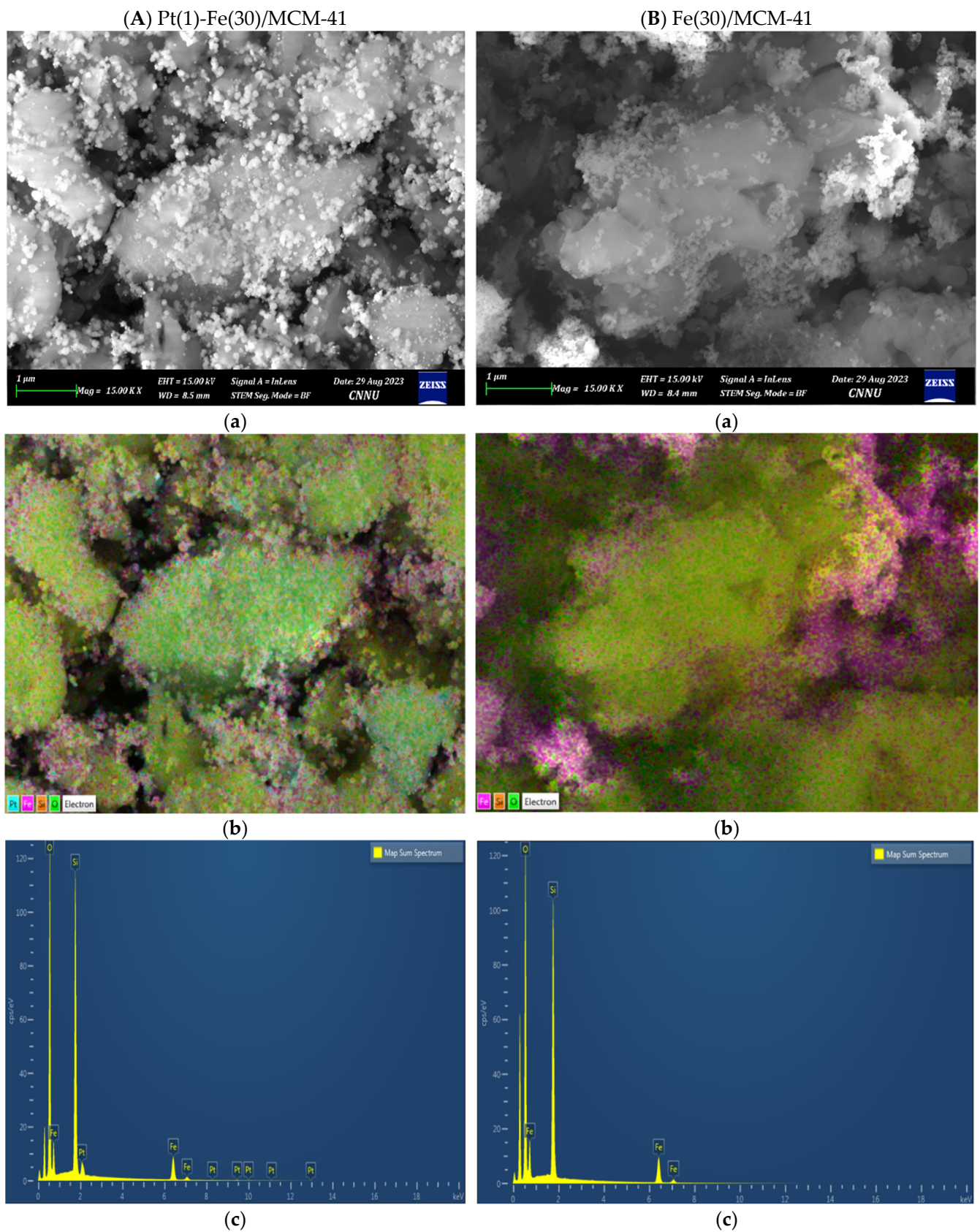


**Figure 7.** (A) FESEM (Aa) image, (Ab) mapping, and (Ac) EDS characteristic peaks of fresh Pt(1)-Fe(30)/MCM-41 and (B) FESEM (Ba) image, (Bb) mapping, and (Bc) EDS characteristic peaks of fresh Fe(30)/MCM-41 [42].

### 2.3. Characterization of Carbon Deposited on the Catalyst

Figure 8 shows the XRD patterns of the Pt(1)-Fe(30)/MCM-41 post-reaction. The lattice planes of the C(002) at  $2\theta = 26.30^\circ$  and the C(101) at  $2\theta = 43.25^\circ$  are attributed to the growth of graphitic-like structures [43], which are attributable to the presence of filamentous carbon. Additionally, the diffraction peaks at  $2\theta = 45.00^\circ$ ,  $50.01^\circ$ , and  $64.99^\circ$  are assigned to  $\text{Fe}_3\text{C}$ . It is assumed that some Fe particles gradually react with carbon to generate  $\text{Fe}_3\text{C}$  during CDM. Awadallah et al. [7] reported that  $\text{Fe}_2\text{O}_3$  in the catalyst would be reduced stepwise with CDM in the following order:  $\text{Fe}_2\text{O}_3 \rightarrow \text{Fe}_3\text{O}_4 \rightarrow \text{FeO} \rightarrow \text{Fe}$  and  $\text{Fe}_3\text{C}$ . The intensity ratio of C(101)/C(002) is attributable to the order of graphitic layers in the carbonaceous materials [44]. A lower ratio (C(101)/C(002) = 0.64) indicates a higher order of the structure. Moreover, after the reaction, the Pt(1)-Fe(30)/MCM-41 catalyst generated a strong and intense (002) diffraction peak. This suggests that CNT production is more active and that there are fewer defects in the CNT structure [45]. Figure 9 shows the TEM images of the deposited carbon over the Pt(1)-Fe(30)/MCM-41 catalyst after CDM at  $700^\circ\text{C}$  for 6.7 h. As shown in Figure 9a–d, the catalyst produced two kinds of carbon nanotubes: multiwalled CNTs (MWCNTs) and bamboo-shaped CNTs. This is attributed to the dissolution of carbon atoms into nanometal particles with diameters of 10–75 nm, which precipitate at the ends rear to generate the nanometal particles to grow filamentous carbon away from the catalyst surface, depending on the strength of the metal–support interaction [16]. It was found that noticeable nanometal particles were embedded into the tip of the nanotube, which had a tubular MWCNT structure with a hollow core diameter of 14.1 nm and a wall thickness of 7.8 nm, and 16 layers of graphene. Thus, it can be inferred that the growth of MWCNTs is due to a tip-growth mechanism [41,46], which involves the decomposition of  $\text{Fe}_3\text{C}$  into Fe and carbon. It is believed that MWCNTs may be formed as supersaturated carbon dissolved in Fe or Pt nanoparticles located on the external surfaces of the MCM-41 carrier. The Raman spectra also provide useful information about the crystallinity and structural disorder of the carbon nanotubes.

Figure 10 shows the Raman spectra of the as-produced MWCNTs after CDM over Pt(1)-Fe(30)/MCM-41 at  $700^\circ\text{C}$  for 6.7 h. Three well-resolved Raman bands were observed for this catalyst. The bands observed at  $1336\text{ cm}^{-1}$ ,  $1568\text{ cm}^{-1}$ , and  $267\text{ cm}^{-1}$  in the Raman spectrum were named the D band, G band, and 2D ( $G'$ ) band, respectively. The D band at  $1336\text{ cm}^{-1}$  was attributed to the D band of the  $\text{sp}^2$  carbon material and was a result of the carbon disorder, which caused wall defects and lattice distortions in the carbon structures [47]. The G band at  $1568\text{ cm}^{-1}$  was assigned to the crystalline graphitic carbon [48]. The 2D ( $G'$ ) band at  $2678\text{ cm}^{-1}$  was due to a second-order two-phonon process related to the formation of graphene layers. The intensity of the G band and 2D band confirmed the formation of multi-layer graphene sheets. An intense 2D band was observed for the disordered carbon nanomaterials [49]. Additionally, the  $I_D/I_G$  ratio intensity provided valuable information about the crystallinity as well as the graphitization degree of the CNTs [50]. With an  $I_D/I_G$  ratio of (Figure 10), it is evident that the Pt(1)-Fe(30)/MCM-41 catalyst produces MWCNTs with a high degree of crystallinity and graphitization.

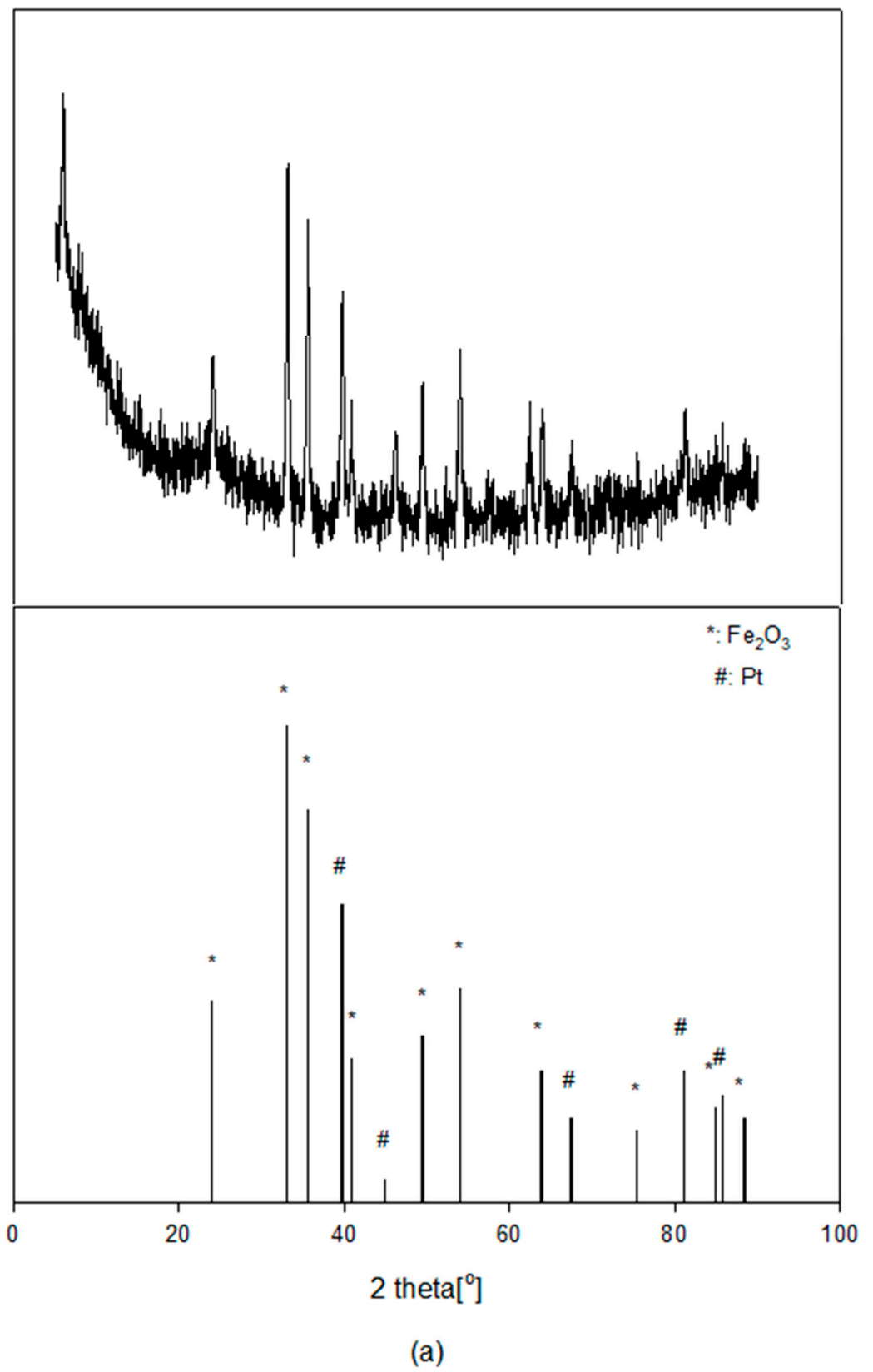


Figure 8. Cont.

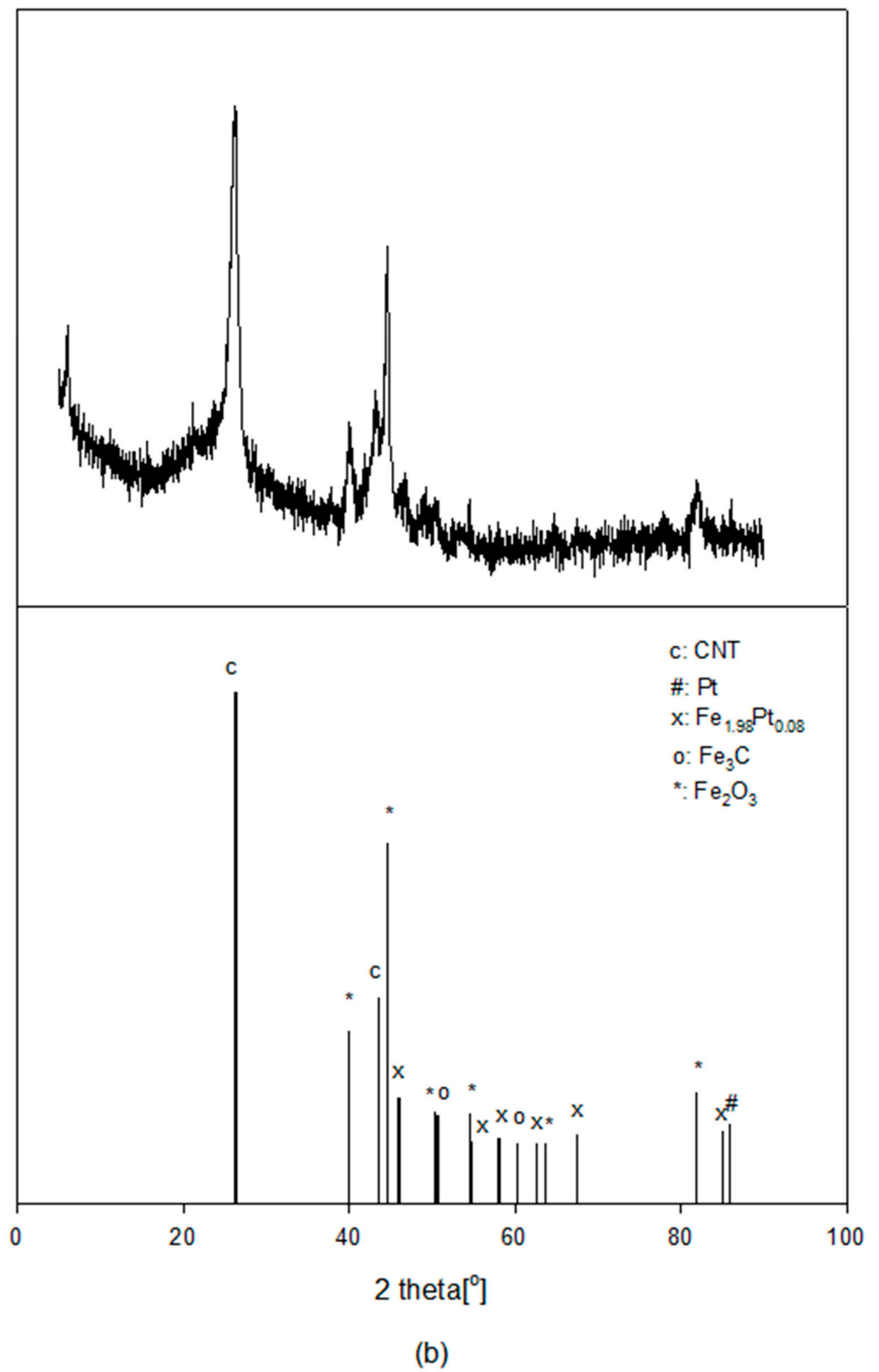
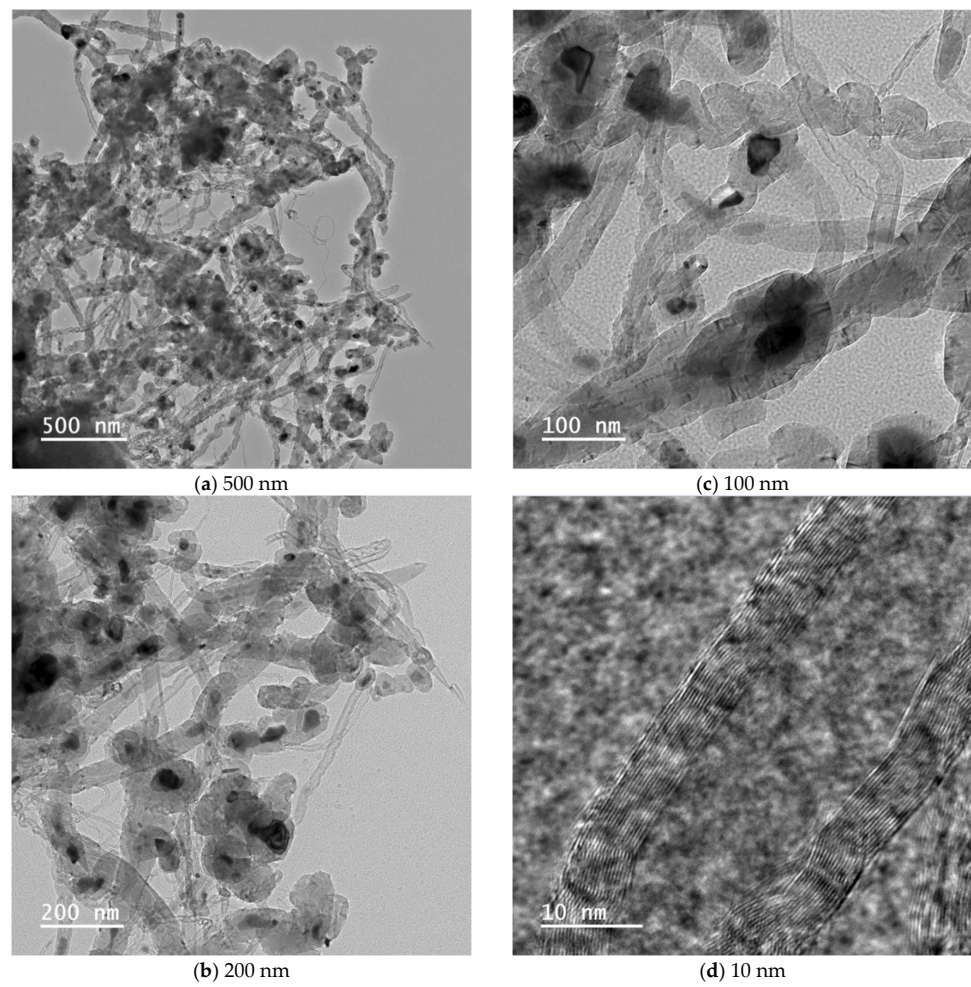
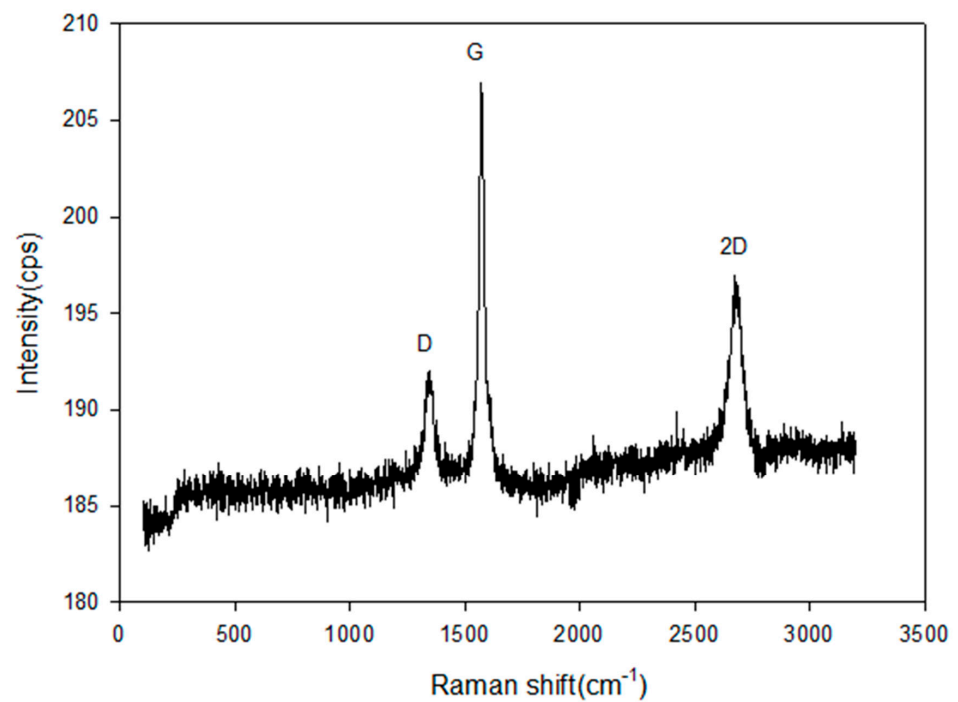


Figure 8. XRD patterns of Pt(1)-Fe(30)/MCM-41 catalysts (a) before and (b) after the reaction.



**Figure 9.** FETEM images at (a) 500 nm, (b) 200 nm, (c) 100 nm, and (d) 10 nm of Pt(1)-Fe(30)/MCM-41 after the reaction.



**Figure 10.** Raman spectra of Pt(1)-Fe(30)/MCM-41 after the reaction.

### 3. Materials and Methods

#### 3.1. Catalyst Preparation

The reagent used to prepare the catalyst was a special reagent with 99.999% purity from Sigma-Aldrich (St. Louis, MO, USA) products. The Pt(1)-Fe(30)/MCM-41 catalyst was prepared using the following standard support method (the numbers in parentheses indicate the percentage of weight carried). Following the dissolution of 0.002 g, 0.295 g, and 0.124 g of Pt(NO<sub>3</sub>)<sub>2</sub>·H<sub>2</sub>O (Sigma-Aldrich, St. Louis, MO, USA) and Fe(NO<sub>3</sub>)<sub>3</sub>·9H<sub>2</sub>O (Sigma-Aldrich, St. Louis, MO, USA), Ni(NO<sub>3</sub>)<sub>2</sub>·6H<sub>2</sub>O (Sigma-Aldrich, St. Louis, MO, USA), respectively, in ethanol, the reactor was filled with 0.1 g of MCM-41 (Sigma-Aldrich, St. Louis, MO, USA) carrier, which is a mesoporous material with a hierarchical structure from a family of aluminosilicate and silicate solids, and it was mixed uniformly with a stirrer for 5 h. The obtained precipitate was filtered and dried in a dryer at 100 °C for 24 h. The dried sample was calcined at 773 K for 5 h in an electric furnace (Eyela, TMF-1000) to create the Pt(1)-Fe(30)/MCM-41, Fe(30)/MCM-41, Pt(1)-Ni(20)/MCM-41, Ni(20)/MCM-41, and Pt(1)/MCM-41 catalysts, and the calcined sample was ground through a 150–200 mesh for use.

#### 3.2. Catalyst Characterization

The XRD data were obtained using a Panalytical (Malvern, UK) Empyrean 3D high-resolution X-ray diffractometer (Cu K $\alpha$  radiation,  $\lambda = 1.5419 \text{ \AA}$ ; 40 kV, 30 mA). The XPS spectra were obtained with AlK $\alpha$  X-rays in operating conditions of  $1 \times 10^{-9}$  mbar and 1.75 keV using an HP-X-ray photoelectron spectrometer (Thermo Scientific (Waltham, MA, USA) K-Alpha+). FESEM images and mapping images were obtained using a Zeiss Sigma (Livonia, MI, USA) 500 model field emission scanning microscope, and the chemical composition of the catalyst was analyzed using an EDS detector (Livonia, MI, USA). FETEM images were obtained using Jeol Jem-2100F at an acceleration voltage of 200 kV. Raman spectra were obtained using a Lazer Raman spectrophotometer (NRS-5100, Jasco, Oklahoma City, OK, USA).

#### 3.3. Catalyst Performance

The catalytic reaction was performed using a fixed-bed flow reactor under atmospheric pressure. About 0.05 g of powdered catalyst was placed on the quartz cotton in the reactor, using a quartz reactor with an internal diameter of 10 mm and a length of 0.3 m. Subsequently, pure methane was supplied to the reactor at a gas hourly space velocity (GHSV) of  $4.2 \times 10^4 \text{ CH}_4 \text{ mL/g}_{\text{cat}} \cdot \text{h}$  under reaction conditions of 973 K and 1 atm. Using a PID controller, the temperature of the reactor was controlled within  $\pm 1 \text{ K}$  by placing a K-type thermocouple on the catalyst in the reactor. After purging the reactant using a pressure gauge attached to each cylinder, the composition of the reactant was controlled using a mass flow meter. The product was analyzed using TCD with a molecular sieve 5 A column connected to the GC (Shimadzu Co., Model 14B, Kyoto, Japan). The catalyst was employed by reducing the hydrogen temperature to 773 K for 5 h at a flow rate of 20 mL/min before the reaction, and then increasing the reaction temperature at a rate of 283 K/min. The CH<sub>4</sub> conversion and H<sub>2</sub> yield of each catalyst were calculated according to the following equation:

$$\text{CH}_4 \text{ conversion}(\%) = \frac{\text{moles of CH}_4 \text{ converted}}{\text{moles of input CH}_4} \times 100 \quad (7)$$

$$\text{H}_2 \text{ yield}(\%) = \frac{\text{moles of H}_2 \text{ produced}}{2 \times \text{moles of input CH}_4 \text{ in the feed}} \times 100 \quad (8)$$

### 4. Conclusions

The CDM reaction was performed with Pt(1)-Fe(30)/MCM-41 and Fe(30)/MCM-41 catalysts using a fixed-bed flow reactor under atmosphere to investigate the methane

conversion and the yield of hydrogen and CNTs. The addition of 1 wt% Pt promoter to Ni(20)/MCM-41 had no significant effect on the methane conversion and hydrogen yield of CDM, but had a significant effect on Fe(30)/MCM-41. The hydrogen yield of Pt(1)-Fe(30)/MCM-41 was 3.2 times higher than that of Fe(30)/MCM-41. The fine nano-sized Fe and Pt particles created by appropriate metal-carrier interactions of the Pt(1)-Fe(30)/MCM-41 and Fe(30)/MCM-41 catalyst were dispersed well in the MCM-41 carrier, and most Fe species in fresh Pt(1)-Fe(30)/MCM-41 were present as Fe<sub>2</sub>O<sub>3</sub> crystallite. The addition of 1 wt% Pt to the Fe(30)/MCM-41 catalyst also increased the atomic percentage of Fe<sub>2p</sub>, which increased from 13.39% to 16.14%, and the Fe<sub>2p<sub>1/2</sub></sub> core electron levels of Fe<sup>0</sup> and Fe<sup>2+</sup> chemically shifted to lower energies (0.2 eV and 0.1 eV, respectively) than those of Fe(30)/MCM-41. Accordingly, Fe ions of Pt(1)-Fe(30)/MCM-41 are more easily reduced than those in Fe(30)/MCM-41. The Fe, Pt, Si, and O nanoparticles were uniformly distributed on the surface of the Pt(1)-Fe(30)/MCM-41 and Fe(30)/MCM-41 catalyst. The Pt(1)-Fe(30)/MCM-41 also created 1.8 times smaller nano-sized iron particles than those of the Fe(30)/MCM-41 catalyst, resulting in a higher dispersion on the MCM-41 surface due to the suitable metal-carrier interaction. The Pt(1)-Fe(30)/MCM-41 produced multiwalled and bamboo-shaped CNTs with high crystallinity and graphitization degrees using the tip-growth mechanism, with an I<sub>D</sub>/I<sub>G</sub> ratio of 0.93 and a C(101)/C(002) ratio of 0.64.

**Funding:** This research received no external funding.

**Data Availability Statement:** Data are contained within the article.

**Conflicts of Interest:** The authors declare no conflicts of interest.

## References

1. Abbas, H.F.; Daud, W.M.A.W. Hydrogen production by methane decomposition: A review. *Int. J. Hydrogen Energy* **2010**, *35*, 1160–1190. [[CrossRef](#)]
2. Ashik, U.P.M.; Wan Daud, W.M.A.; Hayashi, J.-I. A review on methane transformation to hydrogen and nanocarbon: Relevance of catalyst characteristics and experimental parameters on yield. *Renew. Sustain. Energy Rev.* **2017**, *76*, 743–767. [[CrossRef](#)]
3. Surendran, S.; Pathan, M.; Walke, P.; Syam, K.R.; Babu, P.G.; Poojary, N.; Sharma, R. Green synthesis and characterization of multiwall carbon nanotubes from sugarcane bagasse as a biogenic catalyst via chemical vapour deposition method using LPG as hydrocarbon source. *Mater. Lett.* **2024**, *359*, 135904–135908. [[CrossRef](#)]
4. Torres, D.; Pinilla, J.L.; Lázaro, M.J.; Moliner, R.; Suelves, I. Hydrogen and multiwall carbon nanotubes production by catalytic decomposition of methane: Thermogravimetric analysis and scaling-up of FeMo catalysts. *Int. J. Hydrogen Energy* **2014**, *39*, 3698–3709. [[CrossRef](#)]
5. Otsuka, K.; Takenaka, S.; Ohtsuki, H. Production of pure hydrogen by cyclic decomposition of methane and oxidative elimination of carbon nanofibers on supported-Ni-based catalysts. *Appl. Catal. A* **2004**, *273*, 113–124. [[CrossRef](#)]
6. Yao, Y.; Liu, X.; Hildebrandt, D.; Glasser, D. Fisher-Tropsch Synthesis Using H<sub>2</sub>/CO/CO<sub>2</sub> Syngas Mixtures over an Iron Catalyst. *Ind. Eng. Chem. Res.* **2011**, *50*, 11002–11012. [[CrossRef](#)]
7. Awadallah, A.E.; Aboul-Enein, A.A.; El-Desouki, D.S.; Aboul-Gheit, A.K. Catalytic thermal decomposition of methane to CO<sub>x</sub>-free hydrogen and carbon nanotubes over MgO supported Bimetallic group VIII catalysts. *Appl. Surf. Sci.* **2014**, *96*, 100–107. [[CrossRef](#)]
8. Zhao, R.; Du, X.; Cao, K.; Gong, M.; Li, Y.; Ai, J.; Ye, R.; Chen, R.; Shan, B. Highly dispersed Fe-decorated Ni nanoparticles prepared by atomic layer deposition for dry reforming of methane. *Int. J. Hydrogen Energy* **2023**, *48*, 28780–28791. [[CrossRef](#)]
9. Zhao, Y.; Yuan, S.; Deng, J.; Li, C.; Feng, Y.; Xie, X.; Li, N. Investigation on carbon deposition deactivation of Fe-Ni-Ca/Al<sub>2</sub>O<sub>3</sub> catalyst under volatiles reforming of biomass pyrolysis. *J. Anal. Appl. Pyrolysis* **2022**, *168*, 105778–105791. [[CrossRef](#)]
10. Estephane, J.; Aouad, S.; Hany, S.; El Khoury, B.; Gennequin, C.; El Zakhem, H.; El Nakat, J.; Aboukaïs, A.; Abi Aad, E. CO<sub>2</sub> reforming of methane over NiCo/ZSM5 catalysts. Aging and carbon deposition study. *Int. J. Hydrogen Energy* **2015**, *40*, 9201–9208. [[CrossRef](#)]
11. Özdemir, H.; Öksüzömer, M.A.F.; Gürkaynak, M.A. Preparation and characterization of Ni based catalysts for the catalytic partial oxidation of methane: Effect of support basicity on H<sub>2</sub>/CO ratio and carbon deposition. *Int. J. Hydrogen Energy* **2010**, *35*, 12147–12160. [[CrossRef](#)]
12. Wua, H.; Liua, J.; Liu, H.; Hea, D. CO<sub>2</sub> reforming of methane to syngas at high pressure over bi-component NiCo catalyst: The anti-carbon deposition and stability of catalyst. *Fuel* **2019**, *235*, 868–877. [[CrossRef](#)]
13. Han, C.; Zhu, X.; Chen, B.; Wang, X. A strategy of constructing the Ni@silicalite-1 catalyst structure with high activity and resistance to sintering and carbon deposition for dry reforming of methane. *Fuel* **2024**, *355*, 129548–129562. [[CrossRef](#)]
14. Pashchenko, D.; Makarov, I. Carbon deposition in steam methane reforming over a Ni-based catalyst: Experimental and thermodynamic analysis. *Energy* **2021**, *222*, 119993–120002. [[CrossRef](#)]

15. Damyanova, S.; Pawelec, B.; Arishtirova, K.; Fierro, J.L.G.; Sener, C.; Dogu, T. MCM-41 supported PdNi catalysts for dry reforming of methane. *Appl. Catal. B Environ.* **2009**, *92*, 250–261. [[CrossRef](#)]
16. Kutteri, D.A.; Wang, I.-W.; Samanta, A.; Li, L.; Hu, J. Methane decomposition to tip and base grown carbon nanotubes and CO<sub>x</sub>-free H<sub>2</sub> over mono- and bimetallic 3d transition metal catalysts. *Catal. Sci. Technol.* **2018**, *8*, 858–869. [[CrossRef](#)]
17. Naikoo, G.A.; Arshad, F.; Hassan, I.U.; Tabook, M.A.; Pedram, M.Z.; Mustaqeem, M.; Tabassum, H.; Ahmed, W.; Rezakazemi, M. Thermocatalytic Hydrogen Production Through Decomposition of Methane—A Review. *Front. Chem.* **2021**, *9*, 736801–736824. [[CrossRef](#)]
18. Pudukkudy, M.; Yaakob, Z.; Jia, Q.; Takriff, M.S. Catalytic decomposition of undiluted methane into hydrogen and Carbon nanotubes over Pt promoted Ni/CeO<sub>2</sub> catalysts. *N. J. Chem.* **2018**, *42*, 14843–14856. [[CrossRef](#)]
19. Karimi, S.; Bibak, F.; Meshkani, F.; Rastegarpanah, A.; Deng, J.; Liu, Y.; Dai, H. Promotional roles of second metals in catalyzing methane decomposition over the Ni-based catalysts for hydrogen production: A critical review. *Int. J. Hydrogen Energy* **2021**, *46*, 20435–20480. [[CrossRef](#)]
20. Shah, N.; Panjala, D.; Huffman, G.P. Hydrogen Production by Catalytic Decomposition of Methane. *Energy Fuels* **2001**, *15*, 1528–1534. [[CrossRef](#)]
21. Takenaka, S.; Shigeta, Y.; Tanabe, E.; Otsuka, K. Methane Decomposition into Carbon Nanofibers over Supported Pd-Ni Catalysts: Characterization of the Catalysts during the Reaction. *J. Phys. Chem. B* **2004**, *108*, 7656–7664. [[CrossRef](#)]
22. Wang, G.; Jin, Y.; Liu, G.; Li, Y. Production of Hydrogen and Nanocarbon from Catalytic Decomposition of Methane over a Ni-Fe/Al<sub>2</sub>O<sub>3</sub> Catalyst. *Energy Fuels* **2013**, *27*, 4448–4456. [[CrossRef](#)]
23. Shen, Y.; Lua, A.C. Synthesis of Ni and Ni-Cu supported on carbon nanotubes for hydrogen and carbon production by catalytic decomposition of methane. *Appl. Catal. B Environ.* **2015**, *164*, 61–69. [[CrossRef](#)]
24. Pudukudy, M.; Yaakob, Z.; Takriff, M.S. Methane decomposition over Pd promoted Ni/MgAl<sub>2</sub>O<sub>4</sub> catalysts for the production of CO<sub>x</sub> free hydrogen and multiwalled nanotubes. *Appl. Surf. Sci.* **2015**, *356*, 1320–1326. [[CrossRef](#)]
25. Tezel, E.; Figen, H.E.; Baykara, S.Z. Hydrogen production by methane decomposition using bimetallic Ni-Fe catalysts. *Int. J. Hydrogen Energy* **2019**, *44*, 9930–9940. [[CrossRef](#)]
26. Mesfera, M.K.A.; Danisha, M.; Shahb, M. Synthesis and optimization of hydrotalcite derived Ni-Fe-Cu based catalysts for catalytic methane decomposition process using the design of experiment approach. *J. Taiwan Inst. Chem. Eng.* **2021**, *128*, 370–379. [[CrossRef](#)]
27. Wang, Y.; Zhang, Y.; Zhao, S.; Zhu, J.; Jin, L.; Hu, H. Preparation of bimetallic catalysts Ni-Co and Ni-Fe supported on activated carbon for methane decomposition. *Carbon Resour. Convers.* **2020**, *3*, 190–197. [[CrossRef](#)]
28. Awadallah, A.E.; Aboul-Enein, A.A.; Deyab, M.A.; Azab, M.A.; Haggag, A.M. Impact of Cr doping on the performance of Ni/Al<sub>2</sub>O<sub>3</sub> catalyst through methane decomposition into CO<sub>x</sub>-free hydrogen and carbon nanomaterials. *Chem. Eng. Res. Des.* **2022**, *186*, 701–712. [[CrossRef](#)]
29. Sun, H.; Ren, S.; Ji, X.; Song, W.; Guo, Q.; Shen, B. Doping Fe and Zn to modulate Ni nanoparticles on IM-5 for methane decomposition to form hydrogen and CNTs. *Int. J. Hydrogen Energy* **2023**, *48*, 13081–13096. [[CrossRef](#)]
30. Al-Fatesh, A.S.; Abdelkader, A.; Osman, A.I.; Lanre, M.S.; Fakeeha, A.H.; Alhoshan, M.; Alanazi, Y.M.; Awadallah, A.E.; Rooney, D.W. Non-supported bimetallic catalysts of Fe and Co for methane decomposition into H<sub>2</sub> and a mixture of graphene nanosheets and carbon nanotubes. *Int. J. Hydrogen Energy* **2023**, *48*, 26506–26517. [[CrossRef](#)]
31. Zhao, X.S.; Lu, G.Q.; Millar, G.J. Advances in Mesoporous Molecular Sieve MCM-41. *Ind. Eng. Chem. Res.* **1996**, *35*, 2075–2090. [[CrossRef](#)]
32. Kiani, M.R.; Kamandi, R.; Nozarian, K.; Rahimpour, M.R. Introducing a novel catalyst for efficient conversion of CO<sub>2</sub> into syngas through reverse-water-gas-shift (RWGS) reactions based on highly mesoporous structures MCM-41: Influence of the Fe incorporation. *Energy Convers. Manag.* **2024**, *304*, 118247–118263. [[CrossRef](#)]
33. Lopez, L.; Montes, V.; Kušar, H.; Cabrera, S.; Boutonnet, M.; Järås, S. Syngas conversion to ethanol over a mesoporous Cu/MCM-41 catalyst: Effect of K and Fe promoters. *Appl. Catal. A Gen.* **2016**, *526*, 77–83. [[CrossRef](#)]
34. Pawelec, B.; Damyanova, S.; Arishtirova, K.; Fierro, J.L.G.; Petrov, L. Structural and surface features of PtNi catalysts for reforming of methane with CO<sub>2</sub>. *Appl. Catal. A Gen.* **2007**, *323*, 188–201. [[CrossRef](#)]
35. Hu, F.; Jin, C.; Lim, K.H.; Li, C.; Song, G.; Bella, Wang, T.; Ye, R.; Lu, Z.-H.; Feng, G.; et al. Promoting hydrogen spillover of NiFe/CeO<sub>2</sub> catalyst with plasma-treatment for CO<sub>2</sub> methanation. *Fuel Process. Technol.* **2023**, *250*, 107873–107884. [[CrossRef](#)]
36. Vanoye, L.; Guicheret, B.; Rivera-Cárcamo, C.; Audevard, J.; Navarro-Ruiz, J.; del Rosal, I.; Gerber, I.C.; Campos, C.H.; Machado, B.F.; Volkman, J.; et al. Deactivation of Pd/C catalysts by irreversible loss of hydrogen spilloverability of the carbon support. *J. Catal.* **2023**, *424*, 173–188. [[CrossRef](#)]
37. Li, M.; Yin, W.; Pan, J.; Zhu, Y.; Sun, N.; Zhang, X.; Wan, Y.; Luo, Z.; Yi, L.; Wang, L. Hydrogen spillover as a promising strategy for boosting heterogeneous catalysis and hydrogen storage. *Chem. Eng. J.* **2023**, *471*, 144691–144714. [[CrossRef](#)]
38. Guo, J.-H.; Li, X.-D.; Cheng, X.-L.; Liu, H.-Y.; Li, S.-J.; Chen, G. The theoretical study of the bimetallic Ni/Pd, Ni/Pt and Pt/Pd catalysts for hydrogen spillover on penta-graphene. *Int. J. Hydrogen Energy* **2018**, *43*, 19121–19129. [[CrossRef](#)]
39. Boudjahema, A.-G.; Bettahar, M.M. Effect of oxidative pre-treatment on hydrogen spillover for a Ni/SiO<sub>2</sub> catalyst. *J. Mol. Catal. A Chem.* **2017**, *426*, 190–197. [[CrossRef](#)]
40. Ai, Q.; Yuan, Z.; Huang, R.; Yang, C.; Jiang, G.; Xiong, J.; Huang, Z.; Yuan, S. One-pot co-precipitation synthesis of Fe<sub>3</sub>O<sub>4</sub> nanoparticles embedded in 3D carbonaceous matrix as anode for lithium ion batteries. *J. Mater. Sci.* **2019**, *54*, 4212–4224. [[CrossRef](#)]

41. Chen, X.; Pang, X.; Fauteux-Lefebvre, C. The base versus tip growth mode of carbon nanotubes by catalytic hydrocarbon cracking: Review, challenges and opportunities. *Carbon Trends* **2023**, *12*, 100273–100289. [[CrossRef](#)]
42. Seo, H.J. Effect of Pt as a Promoter in Decomposition of CH<sub>4</sub> to Hydrogen over Pt(1)-Fe(30)/MCM-41 catalyst. *Appl. Chem. Eng.* **2023**, *4*, 674–678.
43. Zhu, W.Z.; Miser, D.E.; Chan, W.G.; Hajaligol, M.R. Characterization of multiwalled carbon nanotubes prepared by carbon arc cathode deposit. *Mater. Chem. Phys.* **2003**, *82*, 638–647. [[CrossRef](#)]
44. Serrano, D.P.; Botas, J.A.; Fierro, J.L.G.; Guil-López, R.; Pizarro, P.; Gómez, G. Hydrogen production by methane decomposition: Origin of the catalytic activity of carbon materials. *Fuel* **2010**, *89*, 1241–1248. [[CrossRef](#)]
45. Chen, Y.; Riu, D.-H.; Lim, Y.-S. Carbon nanotubes grown over Fe-Mo-Mg-O composite catalysts. *Met. Mater. Int.* **2008**, *14*, 385–390. [[CrossRef](#)]
46. Gohier, A.; Ewels, C.P.; Minea, T.M.; Djouadi, M.A. Carbon nanotube growth mechanism switches from tip- to base-growth with decreasing catalyst particle size. *Carbon* **2008**, *46*, 1331–1338. [[CrossRef](#)]
47. AL-Fatesh, A.S.; Amin, A.; Ibrahim, A.A.; Khan, W.U.; Soliman, M.A.; AL-Otaibi, R.L.; Fakeeha, A.H. Effect of Ce and Co Addition to Fe/Al<sub>2</sub>O<sub>3</sub> for Catalytic Methane Decomposition. *Catalysts* **2016**, *6*, 40. [[CrossRef](#)]
48. Ferrari, A.C. Raman spectroscopy of graphene and graphite: Disorder, electron-phonon coupling, doping and non-adiabatic effects. *Solid State Commun.* **2007**, *143*, 47–57. [[CrossRef](#)]
49. Lespade, P.; Marchand, A.; Couzi, M.; Cruège, F. Caracterisation de materiaux carbonés par microspectrometrie Raman. *Carbon* **1984**, *22*, 375–385. [[CrossRef](#)]
50. Cheng, J.; Zhang, X.; Luo, Z.; Liu, F.; Ye, Y.; Yin, W.; Liu, W.; Han, Y. Carbon nanotube synthesis and parametric study using CaCO<sub>3</sub> nanocrystals as catalyst support by CVD. *Mater. Chem. Phys.* **2006**, *95*, 5–11. [[CrossRef](#)]

**Disclaimer/Publisher's Note:** The statements, opinions and data contained in all publications are solely those of the individual author(s) and contributor(s) and not of MDPI and/or the editor(s). MDPI and/or the editor(s) disclaim responsibility for any injury to people or property resulting from any ideas, methods, instructions or products referred to in the content.